Band alignment and scattering considerations for enhancing the thermoelectric power factor of complex materials: The case of Co-based half-Heusler alloys

Chathurangi Kumarasinghe* and Neophytos Neophytou
School of Engineering, University of Warwick, Coventry, CV4 7AL, United Kingdom

(Received 6 February 2019; revised manuscript received 5 April 2019; published 16 May 2019)

Producing high band and valley degeneracy through aligning of conducting electronic bands is an effective strategy to improve the thermoelectric performance of complex band-structure materials. Half-Heuslers, an emerging thermoelectric material group, has complex band structures with multiple bands that can be aligned through band engineering approaches, giving us an opportunity to improve their power factor. Theoretical calculations to identify the outcome of band engineering usually employ detailed density functional theory for band-structure calculations, but the transport calculations are kept simplistic using the constant relaxation time approximation due to the complications involved with detailed scattering physics. In this work, going beyond the constant relaxation time approximation, we perform an investigation of the benefits of band alignment in improving the thermoelectric power factor under different density of states dependent scattering scenarios. As a test case we consider the Co-based *p*-type half-Heuslers TiCoSb, NbCoSn, and ZrCoSb. First, using simplified effective mass models combined with Boltzmann transport, we investigate the conditions of band alignment that are beneficial to the thermoelectric power factor under three different carrier scattering scenarios: (i) the usual constant relaxation time approximation, (ii) intraband scattering restricted to the current valley with the scattering rates proportional to the density of states as dictated by Fermi's golden rule, and (iii) both intra- and interband scattering across all available valleys, with the rates determined by the total density of states at the relevant energies. We demonstrate that the band-alignment outcome differs significantly depending on the scattering details. Next, using the density functional theory calculated band structures of the half-Heuslers we study their power factor behavior under strain induced band alignment. We show that strain can improve the power factor of half-Heuslers, but the outcome heavily depends on the curvatures of the bands involved, the specifics of the carrier scattering mechanisms, and the initial band separation. Importantly, we also demonstrate that band alignment is not always beneficial to the power factor. In addition, we show that the band structure itself can undergo changes as the bands are aligned in practice, which further affect the band alignment optimization. Our work illustrates the importance of going beyond the constant relaxation time approximation, as well as understanding how the band structure of each material behaves when considering band alignment.

DOI: 10.1103/PhysRevB.99.195202

I. INTRODUCTION

Thermoelectric (TE) materials are capable of directly converting heat into electricity and vice versa, and are useful in power generation from waste heat [1–5]. The ability of a material to produce thermoelectric power efficiently is quantified by the dimensionless figure of merit:

$$ZT = \sigma S^2 T/\kappa, \tag{1}$$

where σ is the electrical conductivity, S is the Seebeck coefficient, T is the temperature, and κ is the thermal conductivity of the material. For a high ZT, a high electrical conductivity, a high Seebeck coefficient, i.e., a high power factor (σS^2), and a low thermal conductivity κ are desirable. However, simultaneous optimization of these parameters remains a challenge due to their complicated adverse interdependencies. Recently emerged advanced thermoelectric materials, such as half-Heusler alloys [6–13], SnSe, PbTe, and BiTe based compounds [14–16], clathrates [17,18], skutterudites [19,20], to name a few, possess complex crystalline and electronic band structures, exhibiting multiple anisotropic valleys with high degeneracies capable of contributing to conduction. Such features can be useful to overcome the unfavorable interdependencies at least of the conductivity and the Seebeck coefficient by application of band-structure engineering approaches to improve the power factor [21–23].

One of the most promising and commonly employed band-structure engineering approaches in multiband materials is to increase the valley or orbital degeneracy near conduction or valence bands edges [24–26], referred to as "band convergence" or "band alignment". The idea is that when multiple bands contribute to transport, the conductivity, and therefore the power factor, will improve. In bulk materials, band structures can be manipulated by applying strain, doping, alloying, and second phasing with other suitable structures [27–31]. At nanoscale, additional means of influence such as modifying the size, shape, and the chemical surrounding, to name a few, are available [32–35].

In addition to good thermoelectric performance, the ideal thermoelectric material should have low toxicity, relatively

*Chathu.Kumarasinghe@warwick.ac.uk

inexpensive elemental composition, good thermal stability, and be easily produced on a large scale. Half-Heusler alloys are one of the few classes of materials that fulfill the above requirements [6,36]. They are known to have impressive power factors, but unfortunately high thermal conductivities [8,36–38]. As a consequence, much work on half-Heuslers focus on lowering of the thermal conductivity by introducing multiscale defects, manipulating grain sizes, and alloying with elements of large mass contrast. High ZT values close to 1.5 have been achieved under moderate temperatures using such techniques [39,40]. Their complex electronic structure, however, provides opportunities to further optimize the inherently good power factors through band-structure engineering.

The majority of theoretical work related to band-structure engineering (as well as material screening), involves calculating the band structures using *ab initio* density functional theory (DFT), which is then used in conjunction with the Boltzmann transport equation (BTE) in the relaxation time approximation to compute the thermoelectric coefficients [6,41]. Due to the complexities in accurate scattering treatment and the variety of scattering mechanisms, it is common to adopt a constant relaxation time (τ) approximation (usually $\tau \approx 10^{-14}$ s is used at 300 K [41,42]). However, it is quite evident that such a simplification will fail and lead to false estimations of the power factor, particularly when multiple bands participate in transport, such as in studies of band-alignment optimization. Simply, while aligning the bands can increase the number of carriers available for conduction, from simple Fermi's golden rule considerations, it can also increase the number of states that carriers scatter into, which hinders the carrier transport. Therefore, the energy dependence of the scattering mechanisms, as well as the specifics of intra- or intervalley scattering considerations are important in identifying if a given band-structure engineering approach leads to an improved power factor, or not [43–45].

In this work we investigate the role of band alignment in improving the power factor in complex band-structure materials, by considering three possible scattering conditions: (i) the commonly employed constant relaxation time (τ_C), (ii) scattering proportional to the density of states of the band, but restricting to only intravalley scattering [$\tau_{IV}(E)$], and (iii) scattering proportional to the total density of states, allowing both intra- and intervalley and inter- and intraband scattering [$\tau_{IIV}(E)$]. We note that one needs to understand the influence of all three scenarios, as to date, there is almost complete lack of understanding, either theoretical or experimental, in providing evidence in the true nature of scattering in these materials.

As a test case, we use the band structures of the Co-based p-type half-Heuslers, TiCoSb, NbCoSn, ZrCoSb, and ZrCoBi, which have multiple valleys (or carrier pockets) with multiple bands, that can be aligned at the valence band edge (VB_0). We show that when attempting to improve the power factor of materials through band alignment, depending on (i) the scattering considerations, (ii) the masses of the aligned bands, (iii) initial band separation, and (iv) the changes that appear in the band structure upon alignment, different outcomes to the power factor are reached. We show that contrary to current view, band alignment is not always beneficial to the power factor, in fact, in some cases it is misalignment that leads to improvements. We then present in detail the conditions for power factor improvements through simplified equations that would prove useful to material scientists. We further consider the use of strain as a band alignment strategy for these half-Heuslers for power factor improvements. We show that strain can indeed align the bands of Heusler materials, and this can result in even up to a 40% improvement in the power factor.

The paper is organized as follows: In Sec. II we describe our theoretical approach. In Sec. III we start with two simple parabolic bands to illustrate optimum conditions for band alignment under the three different carrier scattering considerations. In Sec. IV we first describe simplified, computationally inexpensive nonparabolic effective mass models derived out of DFT calculated bands to identify potential improvements in the power factor of Co-based half-Heuslers as a result of band alignment. Then, in Sec. V, using more computationally expensive DFT and semiclassical Boltzmann transport calculations, we investigate how strain can be used in reality to achieve band alignment. Finally, in Sec. VI we conclude.

II. METHODS

A. Boltzmann transport equation

To compute the thermoelectric coefficients we employ the Boltzmann transport formalism within the relaxation time approximation (RTA). The materials under consideration are described using effective mass approximations (parabolic and nonparabolic), as well as DFT extracted band structures. The thermoelectric coefficient tensors, electrical conductivity $\sigma_{\alpha,\beta}(T, E_F)$ and Seebeck coefficient $S_{\alpha,\beta}(T, E_F)$, are expressed as [46,47]

$$\sigma_{\alpha\beta}(T, E_F) = e^2 \int \Xi_{\alpha\beta}(E)\Big(-\frac{\partial f(E, E_F, T)}{\partial E}\Big)dE, \quad (2)$$

$$S_{\alpha\beta}(T, E_F) = \frac{e\int \Xi_{\alpha\beta}(E)(E - E_F)(-\frac{\partial f(E,E_F,T)}{\partial E})dE}{T\sigma_{\alpha\beta}(T, E_F)}, \quad (3)$$

where e is the charge of an electron and $f(E, E_F, T)$ is the Fermi distribution function at a given temperature T and a chemical potential E_F. The transport distribution (TD) function $\Xi_{\alpha\beta}(E)$, which is a function of carrier energy E, is given by

$$\Xi_{\alpha\beta}(E) = \sum_{i,\mathbf{k}} \tau_{i,\mathbf{k}}(E) v_\alpha(i, \mathbf{k}) v_\beta(i, \mathbf{k}) \delta(E - E_{i,\mathbf{k}}), \quad (4)$$

where i and $\mathbf{k}$ are the band index and the k point, respectively. The electron relaxation time is denoted by $\tau_{i,\mathbf{k}}(E)$ and $v_\alpha(i, \mathbf{k})$ ($\alpha = x, y, z$) represents the αth component of the group velocity $\mathbf{v}(i, \mathbf{k})$ which can be derived from the slope of the bands in the band structure as

$$v(i, \mathbf{k}) = \frac{1}{\hbar}\nabla_{\mathbf{k}} E_{i,\mathbf{k}}. \quad (5)$$

It can be seen from Eqs. (2) and (3) that the conductivity will increase with the TD function, while the Seebeck coefficient has a more complicated relation, with the contribution of higher energies being weighted more. Therefore, the Seebeck coefficient depends on the energy derivative of the TD function. Numerical calculations for the transport coefficients

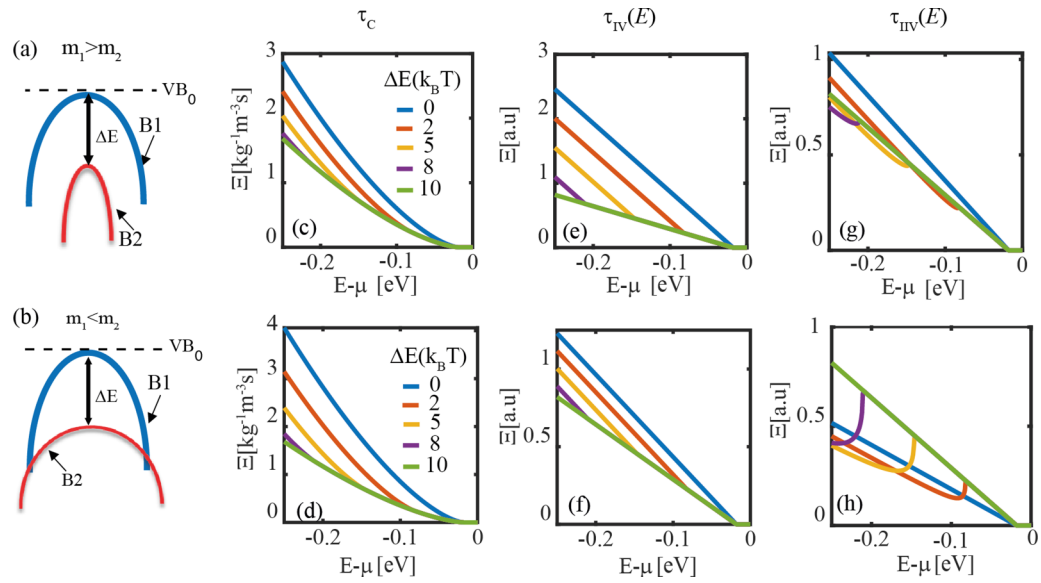

FIG. 1. Transport distribution (TD) functions for different band mass combinations (row-wise) under different scattering scenarios (column-wise). Band B1, which is already aligned with the valence band edge (VB_0), has a mass m_1 and band B2, which is below it has a mass m_2. (a) Schematic representation of aligning a lighter band ($m_1 = 1m_0$, $m_2 = 0.5m_0$) in the first row, and (b) aligning a heavier band ($m_1 = 1m_0$, $m_2 = 2m_0$) in the second row. The displacement between the two bands is given by ΔE. The first row shows the TD functions for aligning a lighter band in case of (c) constant rate of scattering (τ_C), (e) intraband scattering only [$\tau_{IV}(E)$], and (g) inter and intraband scattering [$\tau_{IIV}(E)$]. The second row shows the TD functions for aligning a heavier band in case of (d) constant rate of scattering (τ_C), (f) intraband scattering only [$\tau_{IV}(E)$], and (h) inter- and intraband scattering [$\tau_{IIV}(E)$].

were carried out using the BoltzTraP code [48] (in the case of constant RTA and DFT calculated band structures), in combination with our own developed codes (for the cases of energy-dependent RTA and parabolic/nonparabolic effective mass approximation band structures), as noted below in each described case.

B. *Ab initio* electronic structure calculations

We have performed *ab initio* DFT calculations for the Co-based half-Heuslers, NbCoSn, TiCoSb, ZrCoSb, and ZrCoBi with the QUANTUM ESPRESSO package [49]. Projector augmented wave technique was used with the PBE-GGA functional and a kinetic energy cutoff greater than 60 Ry was used for the wave functions. An energy convergence criterion of 10^{-8} Ry for self-consistency was adopted throughout our calculations. For transport property calculations, a $15 \times 15 \times 15$ Monkhorst-Pack k-point sampling was used for the primitive unit cell with three atoms. Calculations using denser k points were also carried out to confirm the convergence of the results. We calculate an average of transport quantities in x, y, and z crystalline directions, when using DFT derived bands in combination with BoltzTraP. Using the information of three crystallographic orientations, rather than the full anisotropy, is known to give sufficient accuracy in thermoelectric calculations [50–52]. In the DFT calculations, spin-orbit coupling (SOC) effects were not considered. SOC introduces band splitting and changes in the separation between the different valleys, but these effects do not affect our analysis or our qualitative conclusions. In fact, SOC effects are insignificant in the TiCoSn and ZrCoSb cases, whereas in the case of NbCoSn, SOC affects the upper valleys slightly [50,53]. For details of band-structure comparisons with and without SOC see our calculations in the Supplemental Material [54].

C. Parabolic band approximation

For our initial, first-order understanding of the effect of band alignment, we construct a band structure consisting of two parabolic bands [$E = \hbar^2\mathbf{k}^2/(2m)$] with different effective masses, m for each band [as shown in Figs. 1(a) and 1(b)]. We then examine the thermoelectric power factor upon aligning these bands under different scattering RTA scenarios: (i) the commonly employed constant relaxation time $\tau_i(E) = 10^{-14}$ s, (ii) scattering proportional to the density of states of the band, but restricting to only intravalley scattering [$\tau_i(E) \propto 1/\mathrm{DOS}_i(E)$], and (iii) scattering proportional to total density of states, allowing both intra- and intervalley and inter- and intraband scattering [$\tau_i(E) \propto 1/\sum_i \mathrm{DOS}_i(E)$]. We have not considered inter- and intraband scattering with only an intravalley scattering scenario because the above-mentioned scenarios are sufficient to provide a general understanding of the effect of scattering. Since under the parabolic band approximation, the velocity and density of states of each band is $v_i(E) = (2E/m_i)^{1/2}$ and $\mathrm{DOS}_i(E) = 2^{1/2}m_i^{3/2}N_iE^{1/2}/(\pi^2\hbar^3)$, respectively, the TD function for valence bands is reduced to

$$\Xi(E) \propto \sum_i N_i\tau_i(E)m_i^{1/2}E^{3/2}H(-\Delta E_i), \tag{6}$$

where the subscript i indicates each band, ΔE_i indicates the distance to the band edge from the valence band edge, N_i indicates the band degeneracy, and $H(\Delta E_i)$ indicates the Heaviside step function. For conduction bands, $H(-\Delta E_i)$ should be replaced by $H(\Delta E_i)$. We label the band that is

already at the valence band edge VB_0 as B1, and the second, as the "aligning band" B2.

We note that which of the three scattering scenarios is the most appropriate is not possible at this point to determine—it might be that it will be different for different materials, different energies in the same material, or even a combination of all three in the same material. Experimental studies could provide guidance towards understanding the nature of scattering in half-Heuslers, however, data are sparse at the moment, and mostly for alloys and for specific charge densities. Even when it comes to the constant relaxation times, the actual values can differ by orders of magnitude. Indeed, in the Supplemental Material [54] we analyzed data from two experiments for doped-TiCoSb alloys [55,56], which point to larger relaxation times, however, we still use below the more commonly employed $\tau = 10^{-14}$ s. We have also performed *ab initio* electron-phonon scattering calculations using the EPW package [57], for TiCoSb and ZrCoSb in an attempt to understand the nature of scattering, where it seems that the relaxation times follow roughly the downward trend of $1/\mathrm{DOS}(E)$ for TiCoSb, whereas for ZrCoSb a more constant trend followed by a rough $1/\mathrm{DOS}(E)$ at high energies, but extracting further details seems at this point difficult (see the Supplemental Material [54]). Thus, separating the three cases and studying them individually, provides a first-order understanding on the effect of each scattering scenario.

We perform band alignment investigations for the three different scattering rates for two scenarios: (1) band B1 has a heavier mass ($m_1 = 1m_0$) than the aligning band B2 ($m_2 = 0.5m_0$), and (2) B1 has a lighter mass ($m_1 = 1m_0$) compared to the aligning band B2 ($m_2 = 2m_0$) as shown in Figs. 1(a) and 1(b), respectively. The value m_0 is the rest mass of the electron. We assume the band degeneracy $N = 1$ for this study. Band B1 is already aligned with VB_0, and we then bring band B2 gradually closer to B1 by reducing ΔE. We first examine the TD functions to understand the trends of our results, because the influence of the different bands at different ΔE appears there clearly. Figures 1(c)–1(h) show the TD functions for two bands with masses m_1 and m_2 for different levels of alignment in units of k_BT, varying between unaligned ($\Delta E = 10\,k_BT$) to fully aligned ($\Delta E = 0$). Column-wise we show results for the three different scattering situations we have considered, as labeled. Row-wise we show results in the case where we bring a lighter/heavier band into transport, respectively. We note that all our calculations are performed at $T = 300$ K.

III. BAND ALIGNMENT UNDER THE PARABOLIC BAND APPROXIMATION

A. Constant scattering rate and time (τ_C)

Under the constant RTA, $\tau_i(E)$ is a constant and therefore the TD function relation given by Eq. (6) can be simplified to

$$\Xi(E) \propto \sum_i m_i^{1/2}\, E^{3/2}\, H(-\Delta E_i). \tag{7}$$

This indicates that aligning a band of any mass will increase the TD function, resulting finally in an increased conductivity, with the larger masses resulting in larger improvements, a common scenario seen in most band alignment literature. The TD functions for these cases are shown in Figs. 1(c) and 1(d) when bringing in a light/heavy band, respectively. Indeed, it is clear that for the fully aligned cases (blue lines), the TD function is larger when a heavier band is aligned. The thermoelectric coefficients, conductivities, Seebeck coefficients, and power factors, calculated for each scattering scenario, are shown in Fig. 2. Here the three different panels (1–3) show the results for the three different scattering rate scenarios τ_C, $\tau_{IV}(E)$, and $\tau_{IIV}(E)$, respectively. Within each panel, the left column shows the thermoelectric coefficients σ, S, and PF when a lighter band is aligned, whereas the right column when a heavier band is aligned. Focusing on the left panel, Fig. 2.1, which deals with the TE coefficients results under τ_C, we see that as a result of the band convergence, the conductivity increases following the increase in the TD function [Figs. 2.1(a) and 2.1(d)]. The impact of band alignment on the Seebeck coefficient, however, is not significant [Figs. 2.1(b) and 2.1(e)]. The magnitude and sign of the Seebeck coefficient are related to the asymmetry of the electron transport around the Fermi level [58,59], which is indicated by the energy gradient of the TD function. For the range of band effective masses we are concerned with, aligning does not additionally introduce significant asymmetry (or significant change in gradient of the TD function) in the electron transport window around the Fermi level where the PF peak is observed. The resulting power factor shows an improvement upon band alignment (a maximum improvement of 143% when a band of heavier mass is brought to the band edge, as opposed to 69% when a band with lighter mass is aligned), as seen in Figs. 2.1(c) and 2.1(f). Therefore, in the case of a constant relaxation time (τ_C), which is the most commonly employed approximation in theoretical investigations, a power factor improvement is always achieved upon band alignment, with a heavier second band being preferred. As we show further below, this is not the case when $\tau = \tau(E)$.

B. Intraband scattering only [$\tau_{IV}(E)$]

Within Fermi's golden rule, the scattering rate is proportional to the density of available states that a charge carrier can scatter into [43,60,61]. Therefore, it is natural to investigate the effect of such a scattering scenario on the TE coefficients under band alignment. In multivalley multiband materials the selection rules for each scattering mechanism dictate if the carriers are allowed to scatter only within their current band (intraband) in the current valley (intravalley), or whether scattering into states in other bands (interband) and other valleys (intervalley) is also allowed [43–45,62]. For intraband scattering (limited to intravalley in multivalley materials) $\tau_{IV}(E)$, we have $\tau_i(E) \propto 1/\mathrm{DOS}_i(E)$, and the TD function given by Eq. (6) can be simplified to

$$\Xi(E) \propto \sum_i \frac{E}{m_i} H(-\Delta E_i). \tag{8}$$

This indicates again that aligning a band of any mass will increase the TD function, resulting in an increased conductivity. As opposed to the previous τ_C scenario, however, lighter bands benefit transport (since the band mass is now in the

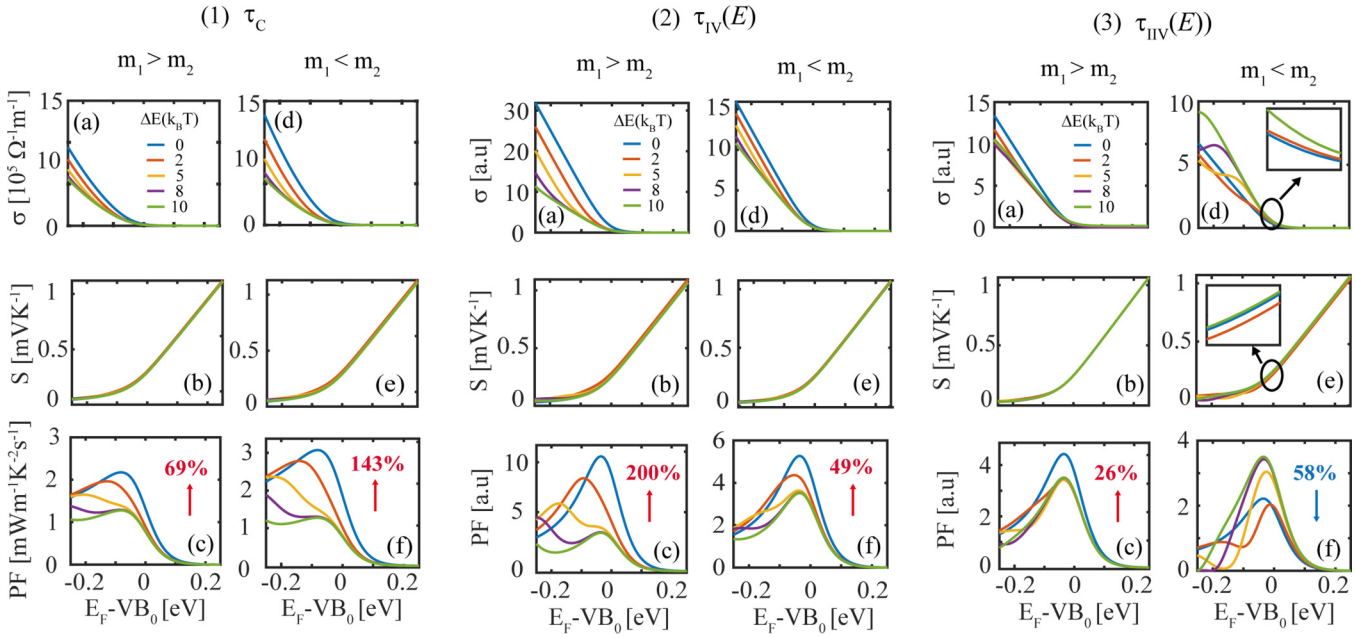

FIG. 2. Thermoelectric coefficients when aligning bands with different mass combinations under three scattering scenarios: Panel 1 for constant rate/time of scattering (τ_C), panel 2 for intraband scattering only [$\tau_{IV}(E)$], and panel 3 for inter- and intraband scattering [$\tau_{IIV}(E)$]. Each panel shows the coefficients: (a) electronic conductivity, (b) Seebeck coefficient, and (c) power factor when the mass of B1 is larger than that of B2, i.e., $m_1 > m_2$ ($m_1 = 1m_0$, $m_2 = 0.5m_0$). (d)–(f) Show the (d) electronic conductivity, (e) Seebeck coefficient, and (f) power factor when the mass of B1 is smaller than that of B2, i.e., $m_1 < m_2$ ($m_1 = 1m_0$, $m_2 = 2m_0$).

denominator), and bringing lighter bands closer to the band edge will provide a higher improvement. This is indicated in Figs. 1(e) and 1(f) for the TD functions in this scattering scenario, where the fully aligned blue line shows largest improvement under light band alignment, in contrast to the τ_C case in Figs. 1(c) and 1(d). Notice that the TD functions in Figs. 1(e) and 1(f) are nonsmooth, highlighting the additional transport component that is added from the second band. The thermoelectric coefficients resulting out of these TD functions as a function of the Fermi level position are shown in the middle panel of Fig. 2. It can be seen that as a result of the band convergence, the conductivity increases [Figs. 2.2(a) and 2.2(d)], the Seebeck coefficient is still not affected noticeably [Figs. 2.2(b) and 2.2(e)], and the resulting power factor shows a large improvement of 200% when a light band is brought in, as opposed to 49% when a heavier band mass is aligned [Figs. 2.2(c) and 2.2(f), respectively]. Therefore, in the case of $\tau_{IV}(E)$ scattering with $\tau_i(E) \propto 1/\mathrm{DOS}_i(E)$, a power factor improvement is always achieved upon band alignment, but now a lighter second band is preferred. Note that in this case the TE coefficients are given in arbitrary units, as we do not consider any specific value for the scattering rate other than its energy dependence.

C. Inter- and intraband scattering [$\tau_{IIV}(E)$]

In this case, carriers are allowed to scatter elastically to the total density of states available at the energy under consideration, without any selection rules, i.e., both inter- and intraband (with inter- and intravalley in multivalley materials) scattering is allowed [$\tau_i(E) \propto 1/\sum_i \mathrm{DOS}_i(E)$]. The TD function relation given by Eq. (6) in this case can be simplified to

$$\Xi(E) \propto \frac{\sum_i m_i^{1/2} E^{3/2} H(-\Delta E_i)}{\sum_i m_i^{3/2} E^{1/2} H(-\Delta E_i)}. \tag{9}$$

From Eq. (9), since the denominator has a higher mass exponent, it can be deduced that upon full band alignment, the TD function will only increase when a light band (B2) is brought close to the band edge and is aligned with a heavier band (B1), i.e., $m_1 > m_2$ (see details in Appendix A). The TD functions for this scattering scenario under bringing in a light/heavy mass are shown in Figs. 1(c) and 1(f), respectively. Here also we assume that ΔE_i is large enough so that initially, before aligning, only B1 contributes to conduction (green lines). When an additional band B2 is gradually brought close to the band edge to be aligned with band B1, three competing effects take place: (1) the presence of the additional conducting states from B2 tends to increase the TD function, (2) the same states increase the scattering out of B1, which tends to reduce the TD function, and (3) scattering from B2 reduces since there are less states to scatter into in B1 at energies closer to VB_0, increasing the TD function. These interdependencies do not allow for the significant improvements in the TD, the conductivity, and the PF that were observed in the previous two scattering scenarios. When $m_1 < m_2$, at the energy where the second band is reached, the TD experiences a sharp drop due to increased scattering [Fig. 1(h)]. This drop is not very notable when $m_1 > m_2$ [Fig. 1(g)]. The thermoelectric coefficients for this scenario are shown in the right panel of Fig. 2, for cases where we bring in a lighter band [Figs. 2.3(a)–2.3(c)], and a heavier band [Figs. 2.3(d)–2.3(f)].

In the first case where $m_1 > m_2$, the conductivity is improved upon band convergence, even though not as much as observed in the previous scattering scenarios. The power factor shows an improvement of only 26% upon full alignment. When a heavier mass is aligned, on the other hand in Figs. 2.3(d)–2.3(f), the conductivity is reduced and as a result, the power factor is reduced (by 58%) due to increased scattering, as opposed to all the previous cases [compare the blue fully aligned with the green unaligned lines in Fig. 2.3(f)]. This indicates that aligning bands is not always advantageous. It is worth mentioning that this reduction is calculated between the $\Delta E = 10\,k_B T$ and $\Delta E = 0$ cases. However, when comparing the power factors in a narrower energy region between the $\Delta E = 2k_B T$ and $\Delta E = 0$ [compare the blue with the red lines in Fig. 2.3(f)], there is a small improvement. This indicates that if there is an improvement to the power factor or not, depends on initial band separation ΔE. As shown in the inset of Fig. 2.3(e), this increase is due to an increase in the Seebeck coefficient. The change in gradient of the TD function, as the B2 approaches the vicinity of VB_0, caused the Seebeck coefficient to reduce slightly [see inset of Fig. 2.3(f)]. Upon full alignment, however, the sharp drop disappears increasing the Seebeck coefficient again. This increase in Seebeck coefficient close to the PF peak overcomes the reduction in conductivity upon full alignment, in this situation [inset of Fig. 2.3(d)]. Note that such nonmonotonic behavior can also be present in the conductivity, with increased number of carriers and reduced scattering from B2 overcoming the disadvantage of increased scattering from B1.

In the case of three bands, where two bands of masses m_2 and m_3 are aligned with a band of mass m_1, the condition for an improved three-band TD function when those three bands are completely aligned compared to the single band TD function given by (see details in Appendix C)

$$m_1 > \frac{\left(m_2^{3/2} + m_3^{3/2}\right)}{\left(m_2^{1/2} + m_3^{1/2}\right)}. \tag{10}$$

From the above equation, we see that in general terms, in the case of $\tau_{\mathrm{IIV}}(E)$, bringing in lighter bands into transport is beneficial for the TD function. Note, however, that this trend is not monotonic when considering the power factor versus ΔE as we will be discussing below.

In order to have a more comprehensive first-order understanding of the benefits of band alignment, we have calculated the power factor using the effective mass approximation for combinations of different band effective mass ratios (m_2/m_1) from 0.1 up to 10, and for band separations (ΔE) of up to $10\,k_B T$, as first adopted by Jeong *et al.* [63]. The maximum power factors for all cases are shown in the color plots of Fig. 3 for the three scattering scenarios τ_C, $\tau_{\mathrm{IV}}(E)$, and $\tau_{\mathrm{IIV}}(E)$. For the ranges we have considered, under a constant rate of scattering (τ_C) in Fig. 3(a), aligning a band with any mass is going to improve the power factor (brighter colors towards the left for smaller ΔE) and aligning heavier bands is more beneficial [brighter colors towards the top of Fig. 3(a)]. This is a result of more states being involved in transport, without however increasing scattering rates, which are kept constant. When energy dependent $\tau_{\mathrm{IV}}(E)$ is considered, the transport in each valley and each band is independent of the other and therefore we observe in Fig. 3(b) [and its zoomed version Fig. 3(c)], that aligning a band with any mass is going to improve the power factor. However, in this case, it is the lighter bands ($m_2/m_1 < 1$) that are more beneficial.

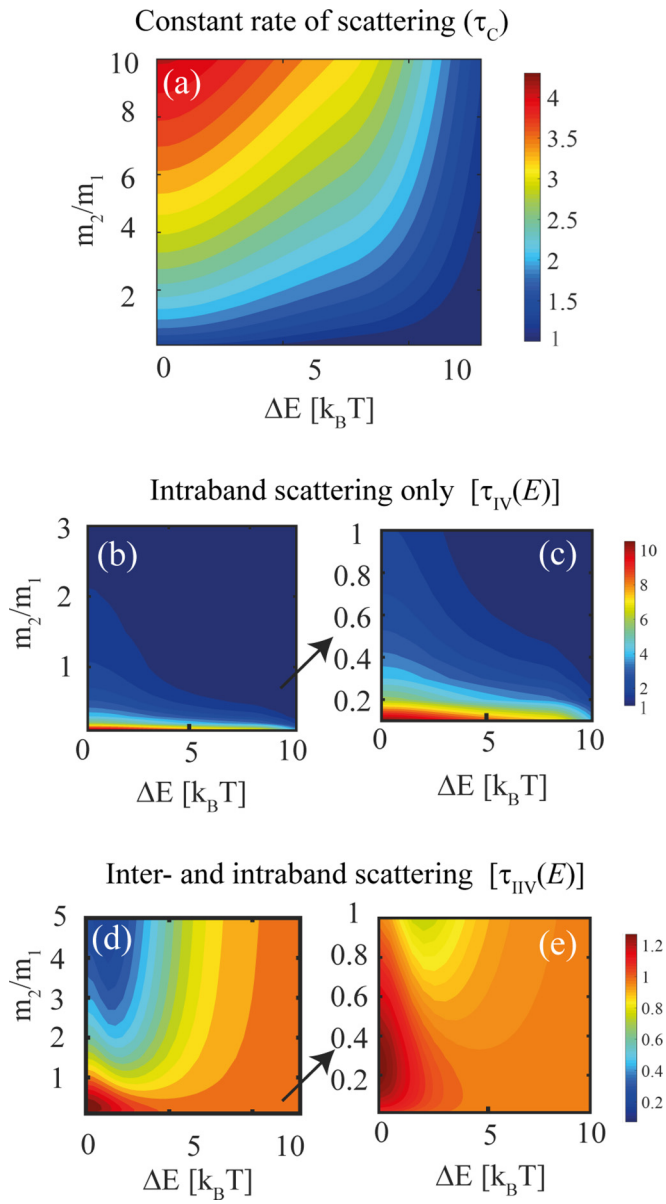

FIG. 3. The color plot shows the maximum power factor (PF) for a two-band system of different combinations of band masses. The power factor is normalized by the maximum PF of the case where the two bands are separated by a large energy interval $\Delta E = 10\,k_B T$ (essentially the single band case). Results as a function of the mass ratio m_1/m_2 (y axis) and band separation ΔE (x axis) are shown. (a) Constant rate of scattering (τ_c) is assumed in the calculation, (b) intraband scattering only [$\tau_{\mathrm{IV}}(E)$], with (c) a zoom of (b). (d) Inter- and intraband scattering [$\tau_{\mathrm{IIV}}(E)$] with (e) a zoom of (d).

When $\tau_{\mathrm{IIV}}(E)$ is considered, interestingly, we no longer have a monotonic relationship between the alignment ΔE, mass ratio, and the power factor improvement. When initially the ΔE is large, i.e., when only one band is initially contributing to conduction within the range we consider ($10\,k_B T$),

aligning masses heavier than the existing mass ($m_2/m_1 > 1$) is going to reduce the power factor, as shown in Fig. 3(d). This shows that, counterintuitively, aligning bands is not always beneficial for the power factor. This is because the benefit of increase in conduction band states is offset by increase in scattering. For $m_2/m_1 > 1$, when ΔE is gradually reduced, the peak power factor is reduced at first and reaches a minimum, but then it experiences an increase (still less than the max power factor at band separation $\Delta E = 10\,k_B T$). One reason for this nonmonotonic behavior is an increase in the Seebeck coefficient closer to VB_0 where the power factor peak is observed as a result of asymmetry in the electron transport introduced by the placement of the second band. Another reason for this nonmonotonic behavior is the increment seen in conductivity as a result of competing effects of increased conduction states and scattering, as ΔE becomes smaller (contribution from B2 keeps increasing with reducing ΔE as a result of reduced number states in B1 to scatter into, closer to VB_0). Therefore, for certain initial smaller ΔE, even under the $m_2/m_1 > 1$ condition, we will observe an improvement in the power factor with both reducing and increasing ΔE due to nonmonotonic behavior in the conductivity and the Seebeck coefficient. Similar nonmonotonic behavior is seen when lighter bands are aligned ($m_2/m_1 > 1$), but unlike for heavier bands, improvements to the power factor can be seen under most m_2/m_1 ratios [areas with colors close to red seen in Fig. 3(e)], even when the initial ΔE is large. Based on Fig. 3(d), note that it is possible to improve the power factor though misaligning the bands (increasing ΔE) for certain m_2/m_1 ratios.

There is an optimum m_2/m_1 ratio which gives the best power factor under $m_2/m_1 < 1$ as seen in Fig. 3(e). To provide an indication about the band mass ratio for the maximum PF, we find the m_2/m_1 that gives the maximum TD function, when bands are fully aligned. The TD function for two bands can be written as

$$\Xi(E) \propto \left(\frac{1+p^{1/2}}{1+p^{3/2}}\right)\frac{E}{m_1}, \tag{11}$$

where $p = m_2/m_1$ (Appendix B). By taking the derivative of $\Xi(E)$ with respect to the mass ratio p, we can find the ratio that maximizes the $\Xi(E)$. We find this value to be $p = 0.25$ and this corresponds to the value of m_2/m_1 that gives the maximum power factor in Fig. 3(e) with the highest improvement seen when the bands are completely aligned ($\Delta E = 0$) under τ_C and $\tau_{IV}(E)$ scattering scenarios. For the mass ranges we have considered, under τ_C, aligning heavy masses are more beneficial, but under $\tau_{IV}(E)$, aligning light bands are more beneficial. Under $\tau_{IIV}(E)$ the outcome is more complex and whether there is an improvement or not depends on masses of the bands and the initial ΔE. In general, for $\tau_{IIV}(E)$, again aligning lighter masses is more beneficial under most initial ΔE values.

IV. NONPARABOLIC BAND (NPB) APPROXIMATION RESULTS FOR Co-BASED HALF-HEUSLERS

Here onwards we start our investigations of band alignment in Co-based half-Heuslers. When examining the DFT extracted band structures of the four half-Heuslers, NbCoSn, TiCoSb, ZrCoSb, and ZrCoBi shown in Fig. 4, it is apparent that multiple bands from several valleys are available close to the VB_0. For instance, in NbCoSn in Fig. 4(a), in addition to the bands at the L and W points that are already aligned at the VB_0, there exist heavy and light bands at the X and Γ points within 0.3 eV of the VB_0. Aligning these bands that are in the vicinity of the VB_0, particularly the bands at the X point that have a large equivalent valley degeneracy of 3, can lead to an improved conductivity and power factor. Similar features that are useful for band-structure engineering strategies to be applied can be seen in the other three materials as well, especially near the VB_0. The TE coefficients for these materials for n-type and p-type cases versus the Fermi level position, extracted numerically using BoltzTraP, under a constant relaxation time τ_C, are shown in Appendix C. From here on, we have selected to use band alignment to further improve the p-type power factor, however, similar studies could be performed for improving the n-type material power factor as well.

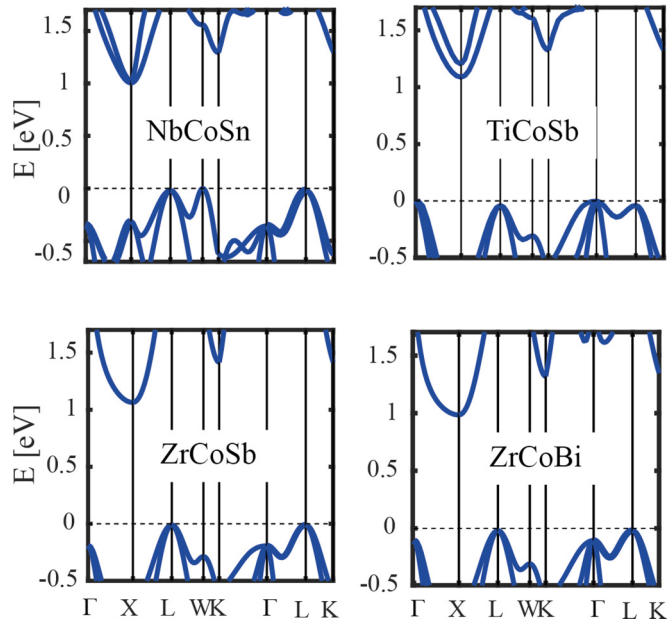

FIG. 4. Band structures of the half-Heuslers NbCoSn, TiCoSb, ZrCoSb, and ZrCoBi.

As a first approach in examining how these materials would behave if certain bands are brought closer, or completely aligned with the VB_0, we pick two of the materials in Fig. 4, namely NbCoSn (because of high initial ΔE between the X and L valleys) and TiCoSb (of a lower initial ΔE between Γ and L). We then used the simple nonparabolic band approximation to create the essential features of the band structures of these materials in the [100] transport direction. Once we form and calibrate our approximate bands to the DFT bands, we can control their alignment at will, without worrying at the moment about how this alignment will be achieved in practice. The $E - \mathbf{k}$ relation for a nonparabolic band is given by

$$E(1+\alpha E) = \frac{\hbar^2 \mathbf{k}^2}{2m}, \tag{12}$$

where α is the nonparabolicity parameter. The parameters $DOS_i(E)$ and $v_i(E)$ that are necessary to calculate the TD

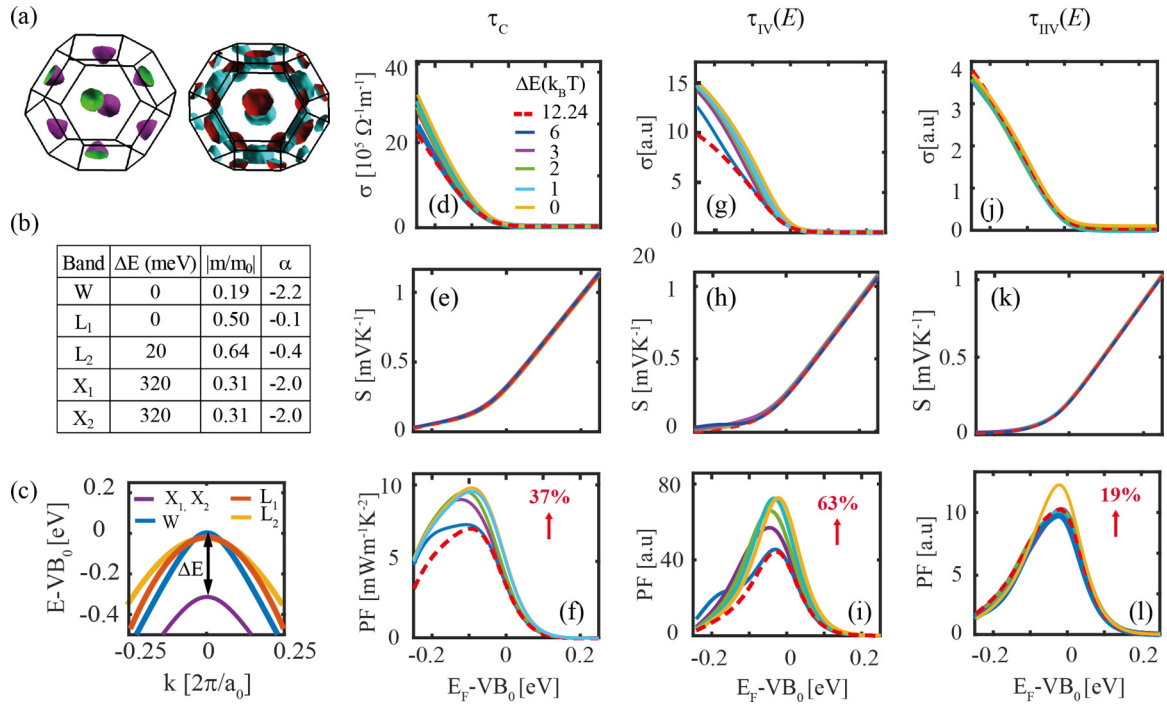

Band	ΔE (meV)	$\lvert m/m_0 \rvert$	α
W	0	0.19	-2.2
L_1	0	0.50	-0.1
L_2	20	0.64	-0.4
X_1	320	0.31	-2.0
X_2	320	0.31	-2.0

FIG. 5. Thermoelectric coefficients for band alignment in NbCoSb described using the nonparabolic band (NPB) approximation, under three different scattering scenarios. (a) The Fermi surface of NbCoSn at 0.1 eV below VB_0. (b) NPB parameters calculated for valence bands at W, L (L_1 and L_2), and X (X_1 and X_2) valleys, assuming transport in the [100] direction. (c) The resulting NbCoSb bands extracted using the NPB approximation. The energy position of bands X_1 and X_2 is shifted by ΔE (in units of k_BT) until it is fully aligned with the VB_0. Column-wise: (d)–(f) Thermoelectric coefficients (σ, S, and PF) calculated using the NPB approximation for NbCoSn under a constant rate of scattering (τ_C). (g)–(i) σ, S, and PF under intraband\intravalley scattering only [$\tau_{IV}(E)$]. (j)–(l) σ, S, and PF under inter- and intraband\inter- and intravalley scattering [$\tau_{IIV}(E)$]. The percentage improvement given is the peak to peak improvement between the $\Delta E = 0$ and $\Delta E = 12.24 k_BT$ (given by the yellow solid line and red dashed lines, respectively).

function using Eq. (6) can be also analytically calculated under the NPB approximation for 3D bands as

$$\mathrm{DOS}_i(E) = \frac{m_i^{3/2}}{\pi^2\hbar^3} N_i \sqrt{2E(1+\alpha_i E)}(1+2\alpha_i E), \tag{13}$$

$$v_i(E) = \sqrt{\frac{2E(1+\alpha_i E) - \Delta E_i}{m_i}} \frac{1}{(1+2\alpha_i E)}. \tag{14}$$

The Fermi surface of NbCoSn at an energy 0.1 eV below the VB_0 is shown in Fig. 5(a). This captures the two bands seen at L and W points of NbCoSn (see band structure in Fig. 4). Despite the fact that the bands are strongly curved, we find that a NPB approximation can fit the bands reasonably well, at least up to 0.25 eV below VB_0. The band structure contains two already aligned bands at the L point (L_1 and L_2) and one band at W (W_1) with equivalent valley degeneracies of 4 and 6, respectively (Fig. 4). The two bands at the X (X_1 and X_2), with equivalent valley degeneracies of 3 are positioned at 315 meV ($12.24 k_BT$ at $T = 300$ K) below VB_0, and these are the bands that we will align with VB_0. The nonparabolic model parameters that describe the relevant bands at X, L, and W valleys are given in the table of Fig. 5(b). Here we assume the [100] direction as the transport direction. Figure 5(c) shows the bands reconstructed using the NPB approximation. To verify the accuracy of the NPB approximation using the parameters that we have extracted for NbCoSn, in Fig. 5(b) we have compared the power factor of the band structure we constructed with that of the DFT band structure using a fully numerical calculation performed using BoltzTraP in Appendix E. Good agreement is found between the NPB and DFT band structures for E_F positioned up to -0.1 eV ($4 k_BT$ into the valence band), which is anyway beyond where the E_F needs to be placed at for maximum PF, or under realistic scenarios. Beyond $E = -0.15$ eV the two methods slightly diverge, signaling that the shape of the actual band structure cannot be mapped to a NBP approximation beyond those energies.

After constructing an equivalent simplified band structure, we now proceed in extracting the electrical conductivity, Seebeck coefficient, and PF for NbCoSn under gradual alignment of bands X_1 and X_2. We extract the TE coefficients under the three different scattering cases we described above (τ_C [Figs. 5(d)–5(f)], $\tau_{IV}(E)$ [Figs. 5(g)–5(i)], and $\tau_{IIV}(E)$ [Figs. 5(j)–5(l)]). The alignment energy step we impose is in units of k_BT as indicated in the caption of Fig. 5(d). With the dashed red line we show the results for the original NPB band structure, before attempting any alignment. Upon band alignment, improvements to the conductivity, and hence to the power factor, can be observed in all three scattering scenarios. No significant variations appears in the Seebeck coefficient. The highest improvement is achieved when the bands are fully aligned (yellow lines, for $\Delta E = 0$). Since the bands we are aligning are effectively lighter than two of the bands that are already aligned at VB_0, the most improvement [63%

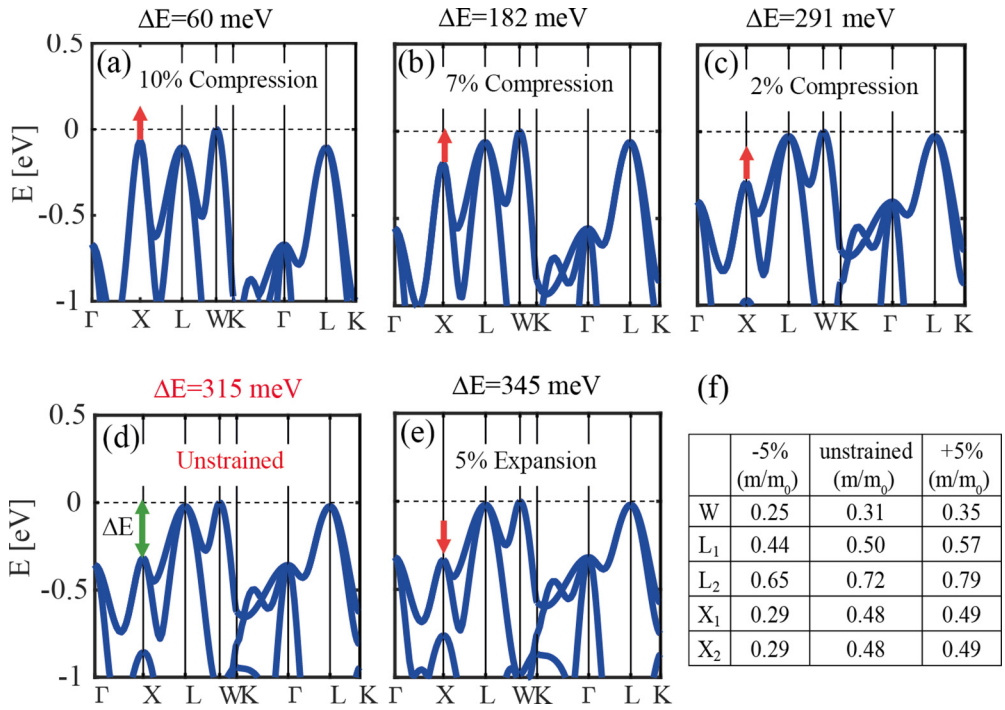

	-5% (m/m_0)	unstrained (m/m_0)	+5% (m/m_0)
W	0.25	0.31	0.35
L_1	0.44	0.50	0.57
L_2	0.65	0.72	0.79
X_1	0.29	0.48	0.49
X_2	0.29	0.48	0.49

FIG. 6. (a)–(e) Application of strain in NbCoSb to align the X valley with the valence band edge. Strain values are as indicated in the figures, with (d) showing the unstrained band structure. (f) The calculated effective masses for the relevant bands at L, W, and X valleys of NbCoSn using the parabolic band approximation for different strain levels [−5% (compressive), unstrained, and +5% (tensile)]. The energy separation ΔE between the X valley and VB_0 are noted above the subfigures.

in Fig. 5(i)] is seen under $\tau_{IV}(E)$ scattering, because states with higher velocities are brought into transport, as discussed earlier. Smaller improvements are achieved in the other two scattering cases, the $\tau_C(E)$ and the $\tau_{IIV}(E)$ [37% in Fig. 5(f) and 19% in Fig. 5(l), respectively], as the advantage of bringing in high velocity states can be utilized in all cases, as explained above.

The corresponding band alignment results using the NPB approximation for the second material we consider, namely TiCoSb, is shown in Appendix F. In summary, improvements to the power factor are seen under all three scattering scenarios for this material as well, with the most improvement [39% in Fig. 15(l)] seen under $\tau_{IIV}(E)$.

V. THE INFLUENCE OF REALISTIC ALIGNMENT THROUGH STRAIN ON THE POWER FACTOR

A. The use of strain to achieve band alignment

In reality, band alignment can be achieved using a variety of methods such as applying strain [64,65], alloying [24,66,67], increasing temperature (as in skutterudites [25] and lead tellurides [68]), etc. Here, for the purposes of our investigation into the influence of band alignment on the PF, we use the easier method within DFT, which is the use of hydrostatic strain, either compressive or tensile. We investigate the effect of strain in the band structures of three of the half-Heuslers we consider, NbCoSn, TiCoSb, and ZrCoSb. In the following sections, for each material, the thermoelectric coefficients were calculated from DFT derived band structures numerically using BoltzTraP (under the constant relaxation time τ_C approximation) and our own codes [for $\tau_{IIV}(E)$] still by using the DFT extracted numerical DOS and velocities (i.e., we do not use either the parabolic, or the nonparabolic, band approximations in this section). Due to difficulty in obtaining valley specific velocities and density of states from DFT, in this section we do not consider the $\tau_{IV}(E)$ scattering case. We use these examples to highlight the different PF observations under different band conditions that can take place. Because our purpose is to provide an indication as to what alignment will do to the PF, and not how alignment can in practice be achieved, in our study we sometimes use strain even up to unrealistic values (i.e., 10% in some cases), until close to full alignment is achieved, for example. Large distortions in lattices could be achieved by alloying, however, due to the larger computational complexity, we perform the calculations using strain.

B. NbCoSn under strain

The bands of NbCoSn can be manipulated with compression and expansion as shown in Figs. 6(a)–6(e). When compressed, the bands at the X point are brought closer to VB_0, reducing ΔE. To fully align, a compressive strain as large as 10% is required. When the material is under tensile strain (expansion), ΔE increases [see red arrows in Figs. 6(a)–6(e) for the energy shift of the bands in each strain case]. It is important to note, however, that the curvatures of the bands also change with strain. The effective masses reduce with compressive strain and increase with tensile strain as documented in the table of Fig. 6(f). Figure 7 shows the TE coefficients conductivity, Seebeck coefficient, and PF for the two scattering cases considered [τ_C (Fig. 7 first column)

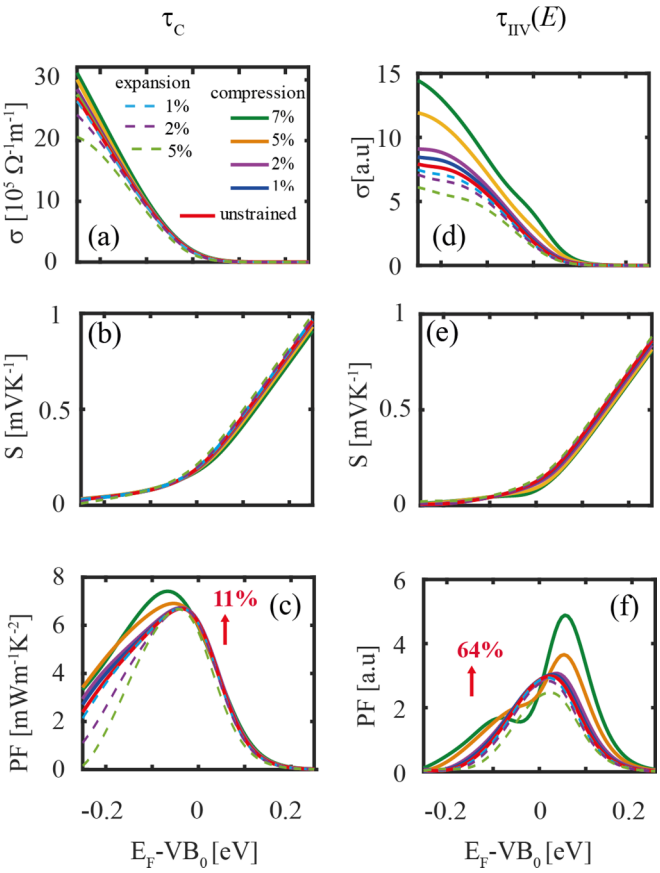

FIG. 7. Column-wise: (a)–(c) Thermoelectric coefficients (σ, S, and PF) calculated using the nonparabolic band (NPB) approximation for NbCoSn under constant rate of scattering (τ_C). (d)–(f) σ, S, and PF under inter- and intraband\inter- and intravalley scattering [$\tau_{IIV}(E)$]. The percentage improvement given is the peak to peak improvement between the unstrained ($\Delta E = 315$ meV) and 7% compressive strain ($\Delta E = 182$ meV), given by the red solid lines and green solid lines, respectively.

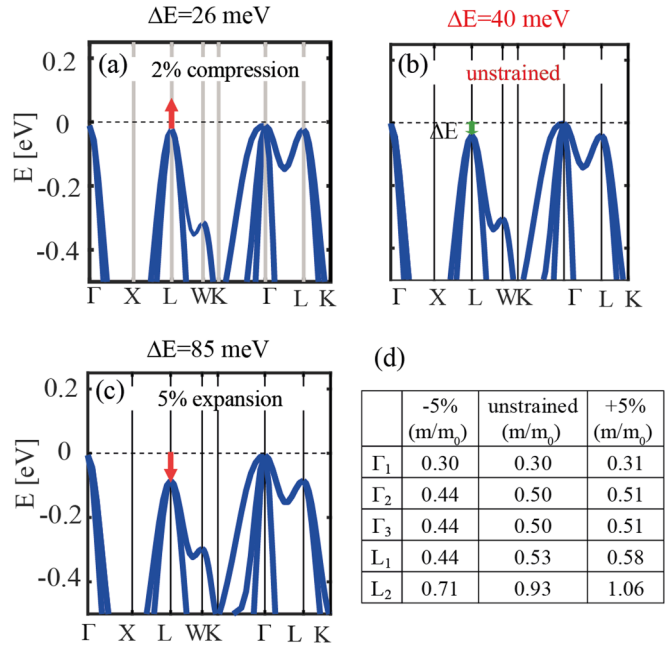

(d)

	-5% (m/m_0)	unstrained (m/m_0)	+5% (m/m_0)
Γ_1	0.30	0.30	0.31
Γ_2	0.44	0.50	0.51
Γ_3	0.44	0.50	0.51
L_1	0.44	0.53	0.58
L_2	0.71	0.93	1.06

FIG. 8. (a)–(c) Application of strain in TiCoSb to align the L valley with the valence band edge. Strain values are as indicated in the figures, with (b) showing the unstrained band structure. (d) The calculated effective masses for the relevant bands at L and Γ valleys of TiCoSb using the parabolic band approximation for different strain levels [−5% (compressive), unstrained, and +5% (tensile)]. The energy separation ΔE between the L valley and VB_0 are noted above the subfigures.

and $\tau_{IIV}(E)$ (Fig. 7 second column)]. The PF is improved in both scattering scenarios under compressive strain, which aligns the bands (solid lines). The improvement, however, is larger in the case of $\tau_{IIV}(E)$ compared to constant scattering τ_C, something that was not observed in the simple NPB analysis we performed earlier in Sec. IV. The fact that the masses reduce with band convergence is unfavorable under a constant scattering rate. It is, however, favorable under $\tau_{IIV}(E)$ as it brings bands with higher velocities that results in less scattering within the transport window, in the cases where ΔE is large. Note here the difference between the simplified NPB approximation extracted TE coefficients as shown earlier in Fig. 5. In that case, the constant relaxation time approximation provided larger benefits to the power factor. However, under the realistic alignment scenario, where additional effects such as the masses reduction with band convergence appear, the $\tau_{IIV}(E)$ scattering scenario gives a better improvement.

C. TiCoSb under strain

The next material we attempt to manipulate with strain is TiCoSb. The energy separation ΔE between bands at L and Γ points of ≈40 meV can be reduced by applying compressive strain, leading to band convergence, as shown in Figs. 8(a)–8(c). The curvatures of all the bands close to VB_0 are reduced with compressive strain and is increased with tensile strain as documented in the table in Fig. 8(d). Figure 9 shows the TE coefficients conductivity, Seebeck coefficient, and PF for the two scattering cases considered [τ_C (Fig. 9 first column) and $\tau_{IIV}(E)$ (Fig. 9 second column)]. Under a constant rate of scattering, we only see 6% improvement when the bands are fully aligned using compressive strain [Fig. 9(c)], but the improvement is 17% under $\tau_{IIV}(E)$ scattering [Fig. 9(f)]. The fact that masses reduce with alignment as before is favorable under the latter scattering scenario, which has contributed to the larger improvement observed. The ΔE value in this situation is only 40 meV ($1.55\,k_BT$ at $T = 300$ K), i.e., bands are almost aligned even without strain. The bands can be fully aligned by applying only ≈ 2% compressive strain (a much more realistic value compared to the ones needed for NbCoSn). Another observation, different compared to NbCoSn, is that the bands we are aligning have higher masses than the bands that are already aligned. Although this is favorable under τ_C, only moderate improvements to the conductivity, and hence to the power factor, are observed in this case, because ΔE is only 40 meV to begin with, and the masses reduce with band alignment. Again, the highest improvement is seen when the bands are fully aligned. The higher improvement that is observed in the PF under $\tau_{IIV}(E)$, is benefited by the fact that bands become lighter as they are aligned. This behavior was seen earlier in Fig. 3(d).

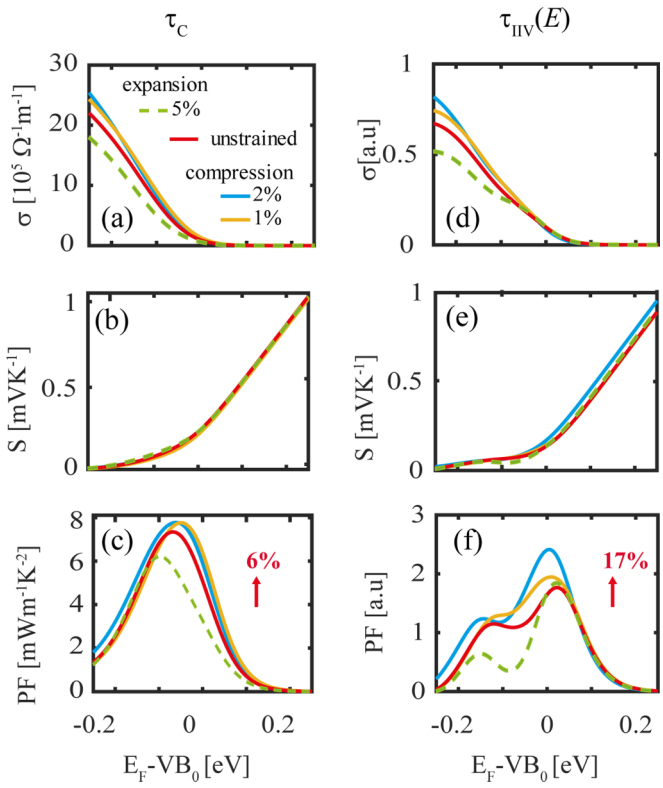

FIG. 9. Column-wise: (a)–(c) Thermoelectric coefficients (σ, S, and PF) calculated using the nonparabolic band (NPB) approximation for TiCoSb under constant rate of scattering (τ_C). (d)–(f) σ, S, and PF under inter- and intraband\inter- and intravalley scattering [$\tau_{IIV}(E)$]. The percentage improvement given is the peak to peak improvement between the unstrained ($\Delta E = 40$ meV) and 2% compressive strain ($\Delta E = 26$ meV), given by the red solid lines and blue solid lines, respectively.

With expansion, which misaligns the bands (increases ΔE), under the $\tau_{IIV}(E)$ scenario, the conductivity and therefore the power factor, increases slightly as seen in Figs. 9(d) and 9(f) (compare the green dotted line with the solid red line), in contrast to τ_C case. Similar nonmonotonic behavior was observed in Fig. 3(d). The percentage improvement values differ from the NPB approximation calculations because of the change in the masses.

D. ZrCoSb under strain

The third material we examine under strain is ZrCoSb (Fig. 10). The bands at the Γ point (Γ_1, Γ_2, and Γ_3) reside 193 meV (or $7.48\,k_BT$ with $T = 300$ K) below VB_0 [Fig. 10(b)]. We attempt to align them with the bands at the L point (L_1 and L_2) at VB_0. As opposed to the previous two materials, band convergence can be achieved by applying tensile strain (expansion), rather than compression [Figs. 10(a)–10(e)]. The already aligned bands L_1 and L_2 become lighter with compressive strain and heavier with tensile strain, as documented in the table of Fig. 10(f). Increase in band masses is beneficial under a constant scattering time τ_C, as explain above in Sec. III. Therefore, in the thermoelectric coefficients in Fig. 11 (τ_C first column [Figs. 11(a)–11(c)]), we find a substantial improvement in the power factor when the bands are fully aligned under τ_C [$\approx 53\%$ in Fig. 11(c) for 7% strain, but $\approx 20\%$ for a more realistic strain value of 3%]. However, this increase in the effective masses and alignment of heavier masses are unfavorable in general under the $\tau_{IIV}(E)$ (second column [Figs. 11(d)–11(f)]) scattering scenario. Therefore, we see a decrease in the power factor by 17% when the bands are aligned under $\tau_{IIV}(E)$ in Fig. 11(f) (compare the red solid line to the blue dashed line). In the case of compressive strain, which further misaligns the Γ valley, but reduces the effective mass of the already aligned bands at L valley, we see an increase in the power factor (red solid line vs blue solid line), as lighter masses are favorable under the $\tau_{IIV}(E)$ scenario, as explained in Sec. III. In the case of 5% compression in Fig. 11(f), therefore, we observe a 12% improvement.

The strain required to completely align the bands can be high as $\approx$10% in NbCoSn and ZrCoSb, which is unrealistic to achieve. However, as seen in Figs. 7, 9, and 11, reducing the distance ΔE is sufficient to see an improvement to the PF, even though fully aligning the bands gives the maximum improvement. Our aim, however, beyond indicating the possibilities of band alignment with strain, was also to demonstrate different scenarios of how the bands' mass can change with alignment, and that this is a factor that can change the expectations out of simple models and needs to be taken into consideration. Importantly, the changes can be different for different materials and strain conditions. In Fig. 12, finally, we show a summary of the power factor improvements with strain of only up to 5% for the three materials we examined (note that we did not perform a strain study for the ZrCoBi since the band structure looks similar to the other half-Heuslers we examined). In Fig. 12(a), under a constant scattering rate, ZrCoSb (green lines in Fig. 12) shows the best performance improvement with tensile strain. Here a $\approx$ 15% improvement in the power factor can be seen even with 1%–2% tensile strain, but the improvement jumps to $\approx$ 30% at 5% strain. TiCoSb shows nearly 5% improvement when 1%–2% compressive strain is applied. The outcomes, however, are different under $\tau_{IIV}(E)$ scattering. It is compressive strain that allows for PF improvements for all three materials under band alignment up to values between 20%–40% at 5% strain, which is quite significant. Tensile strain degrades the performance of ZrCoSb and NbCoSn, but still allows improvements for TiCoSb. Interestingly, in the case of $\tau_{IIV}(E)$ scattering, TiCoSb allows PF improvements with either compressive or tensile strain. However, to achieve these benefits in practice, the precise scattering conditions need to be identified, as different conditions lead to different conclusions.

VI. CONCLUSION

In this work we have provided a comprehensive investigation into the benefits of band alignment (or band convergence) of complex band-structure thermoelectric materials in improving the power factor, by going beyond the constant relaxation time approximation. After a generic investigation using the alignment of simple parabolic bands, we used the actual DFT extracted band structures of the p-type Co-based half-Heuslers NbCoSn, TiCoSb, and ZrCoSb, and used strain to align the various bands that appear in the valence band.

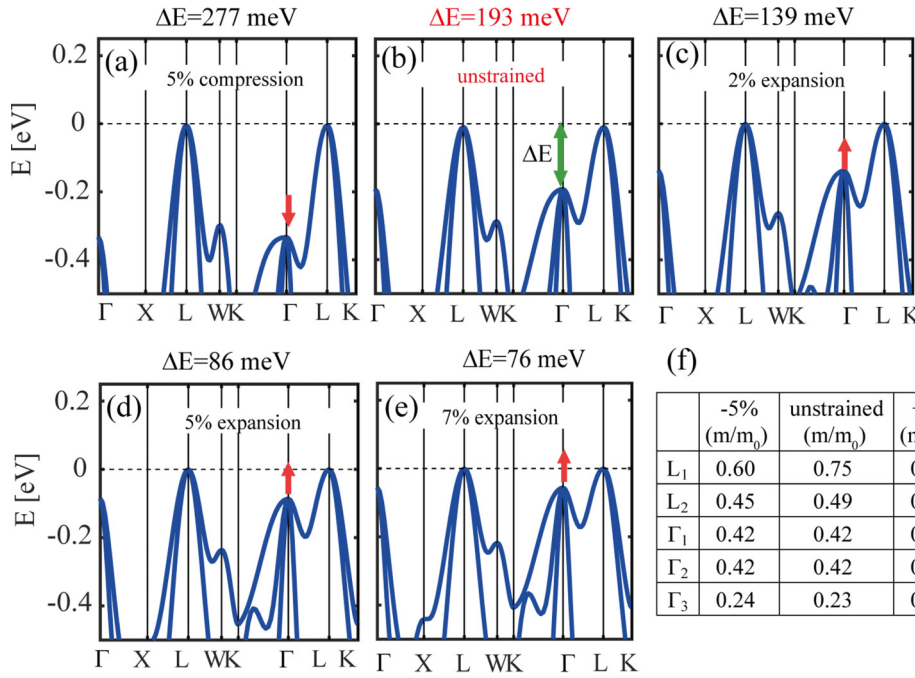

	-5% (m/m_0)	unstrained (m/m_0)	+5% (m/m_0)
L_1	0.60	0.75	0.84
L_2	0.45	0.49	0.54
Γ_1	0.42	0.42	0.41
Γ_2	0.42	0.42	0.41
Γ_3	0.24	0.23	0.21

FIG. 10. (a)–(e) Application of strain in ZrCoSb to align the Γ valley with the valence band edge. Strain values are as indicated in the figures, with (b) showing the unstrained band structure. (f) The calculated effective masses for the relevant bands at L and Γ valleys of ZrCoSb using the parabolic band approximation for different strain levels [−5% (compressive), unstrained, and +5% (tensile)]. The energy separation ΔE between the Γ valley and VB_0 are noted above the subfigures.

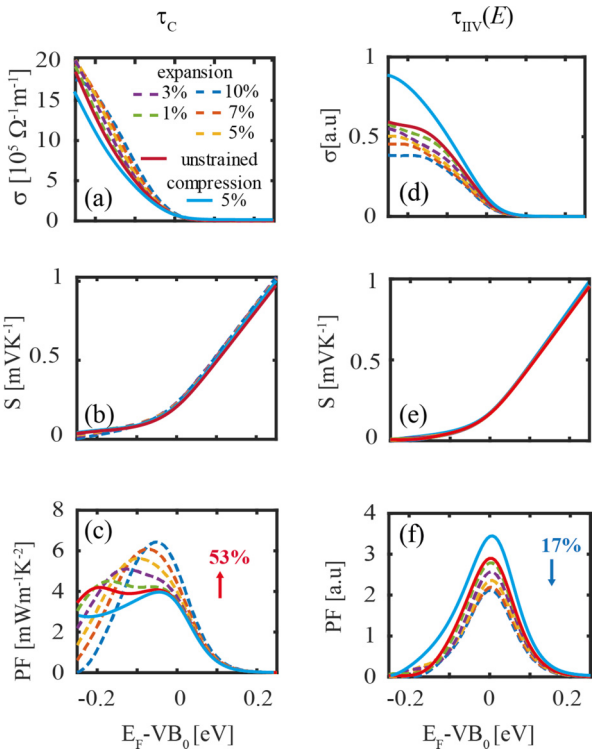

FIG. 11. Column-wise: (a)–(c) Thermoelectric coefficients (σ, S, and PF) calculated using the nonparabolic band approximation for ZrCoSb under constant rate of scattering (τ_C). (d)–(f) σ, S, and PF under inter- and intraband\inter- and intravalley scattering [$\tau_{IIV}(E)$]. The percentage improvement given is the peak to peak improvement between the unstrained ($\Delta E = 193$ meV) and 10% tensile strain ($\Delta E = 27$ meV), given by the red solid lines and blue dashed lines, respectively.

Using the Boltzmann transport equation under the relaxation time approximation, we explored the band alignment effect on the power factor under three different scattering conditions (as the detail scattering physics of half-Heuslers are still not known): (i) constant relaxation time approximation—as is common in most literature, (ii) scattering rates proportional to the density of final states, but under only intraband\intravalley considerations, and (iii) scattering rates proportional to the density of final states, with both inter- and intraband\inter- and intravalley scattering considerations. We showed that the outcome of band alignment can be completely different in each of the different scattering cases. Specifically, constant relaxation time scenarios favor alignment of heavier bands (i.e., bringing

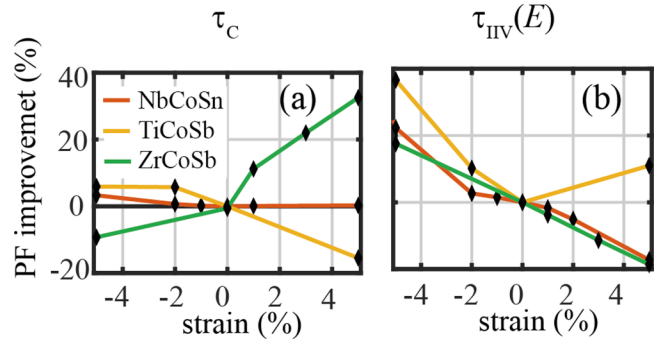

FIG. 12. Percentage improvement of the power factor (from peak to peak) under: (a) Constant rate of scattering (τ_C), and (b) inter- and intraband\inter- and intravalley scattering [$\tau_{IIV}(E)$] versus strain percentage is applied for NbCoSn, TiCoSb, and ZrCoSb. Positive strain indicates expansion while negative strain indicates compression.

heavier bands closer to lighter ones) for larger improvements, as those provide more transport states, but without increase in scattering. On the other hand, alignment of lighter bands is favored for the second scattering situation, where only intraband (and intravalley) scattering is considered, as they provide a small number of carriers with higher velocities, and do not interfere significantly with the scattering of carriers in already aligned bands. The third scattering scenario where both intra- and interband (with inter- and intravalley) scattering is considered, shows a more complicated nonmonotonic relationship between power factor benefits, band separation, and mass ratio. Under this scattering scenario, band convergence can lead to reduction of the power factor in certain cases particularly when heavy bands are aligned, due to increased carrier scattering offsetting the advantage of increase in conducting states. Because of this, we showed that it is the misalignment of the bands, instead of the alignment, which leads to power factor improvements in certain situations. We show that there is an optimum band separation–mass ratio combination, to obtain the best PF improvements. In general, however, we showed that aligning lighter bands favors the power factor in this situation as well. We stressed that aiming for a multiband multivalley band structure does not always improve thermoelectric performance and band alignment strategies need to consider the scattering physics, as they determine whether the power factor will increase or decrease upon alignment. In addition, we point out that under band alignment in realistic material engineering scenarios (i.e., by applying strain), the band curvature can be changed, which adds another complication in determining whether alignment can help or not. In general, however, under constant scattering rate scenarios, bringing in heavy masses helps the power factor, whereas under density of states dependent rates, bringing in lighter masses is what helps. With regards to the application of strain to improve the power factor of half-Heuslers, we showed that application of strain up to 5% can improve the power factor by up to 40%, but whether this is achieved by compression or tension, depends on the specific material and which valleys are aligned. Thus, our work stresses the importance of more accurate theoretical treatment for each material in examining its thermoelectric properties, as the specific details can lead to different conclusions.

ACKNOWLEDGMENT

This work has received funding from the European Research Council (ERC) under the European Union's Horizon 2020 Research and Innovation Programme (Grant Agreement No. 678763).

APPENDIX A: CONDITION FOR TD FUNCTION IMPROVEMENT UNDER $\tau_{\mathrm{IIV}}(E)$ SCATTERING: CASE OF TWO BANDS

When ΔE is large, only the first band B1 contributes to conduction. Therefore, from Eq. (9) the TD function can be written as

$$\Xi(E) \propto \frac{m_1^{1/2}\, E^{3/2}}{m_1^{3/2}\, E^{1/2}}. \tag{A1}$$

When bands B1 and B2 are completely aligned, i.e., $\Delta E = 0$, both B1 and B2 contribute to conduction. Therefore, from Eq. (9), the TD function can be written as

$$\Xi(E) \propto \frac{m_1^{1/2}\, E^{3/2} + m_2^{1/2}\, E^{3/2}}{m_1^{3/2}\, E^{1/2} + m_2^{3/2}\, E^{1/2}}. \tag{A2}$$

To have gains by alignment, we set the TD function given by Eq. (A2) to be larger than what is given by Eq. (A1), which leads to

$$\frac{m_1^{1/2}\, E^{3/2} + m_2^{1/2}\, E^{3/2}}{m_1^{3/2}\, E^{1/2} + m_2^{3/2}\, E^{1/2}} > \frac{m_1^{1/2}\, E^{3/2}}{m_1^{3/2}\, E^{1/2}} \tag{A3}$$

$$\Rightarrow \left(m_1^{1/2} + m_2^{1/2}\right) m_1 > m_1^{3/2} + m_2^{3/2} \tag{A4}$$

$$\Rightarrow m_1 > m_2. \tag{A5}$$

APPENDIX B: BAND MASSES THAT MAXIMIZE THE TD FUNCTION UNDER $\tau_{\mathrm{IIV}}(E)$: CASE OF TWO BANDS

When the bands B1 and B2 are completely aligned, $\Delta E = 0$, and both B1 and B2 contribute to conduction. We set $m_2/m_1 = p$, and from Eq. (9) the TD function can be written as

$$\Xi(E) \propto \frac{m_1^{1/2}\, E^{3/2} + p^{1/2} m_1^{1/2}\, E^{3/2}}{m_1^{3/2}\, E^{1/2} + p^{3/2} m_1^{3/2}\, E^{1/2}} \tag{B1}$$

$$\Rightarrow \Xi(E) \propto \left(\frac{1 + p^{1/2}}{1 + p^{3/2}}\right) \frac{E}{m_1}. \tag{B2}$$

Therefore, the value of the mass ratio p that maximizes the TD function can be obtained by

$$\frac{d}{dp}\left(\frac{1 + p^{1/2}}{1 + p^{3/2}}\right) = 0 \tag{B3}$$

$$\Rightarrow \frac{3(p^{1/2} + 1)p - (1 + p^{3/2})}{(1 + p^{3/2})} = 0 \tag{B4}$$

$$\Rightarrow 2p^{3/2} + 3p - 1 = 0. \tag{B5}$$

The solution to Eq. (B5) gives $p = 0.25$.

APPENDIX C: CONDITION FOR TD FUNCTION IMPROVEMENT UNDER $\tau_{\mathrm{IIV}}(E)$ SCATTERING: CASE OF THREE BANDS

When the separation of bands ΔE is large, only the first band B1 contributes to conduction. Therefore, from Eq. (9) the TD function can be written as

$$\Xi(E) \propto \frac{m_1^{1/2}\, E^{3/2}}{m_1^{3/2}\, E^{1/2}}. \tag{C1}$$

When all three bands B1, B2, and B3 are completely aligned, $\Delta E = 0$, and all B1, B2, and B3 bands contribute to conduction. Therefore, from Eq. (9) the TD function can be written as

$$\Xi(E) \propto \frac{m_1^{1/2}\, E^{3/2} + m_2^{1/2}\, E^{3/2} + m_3^{1/2}\, E^{3/2}}{m_1^{3/2}\, E^{1/2} + m_2^{3/2}\, E^{1/2} + m_3^{3/2}\, E^{1/2}}. \tag{C2}$$

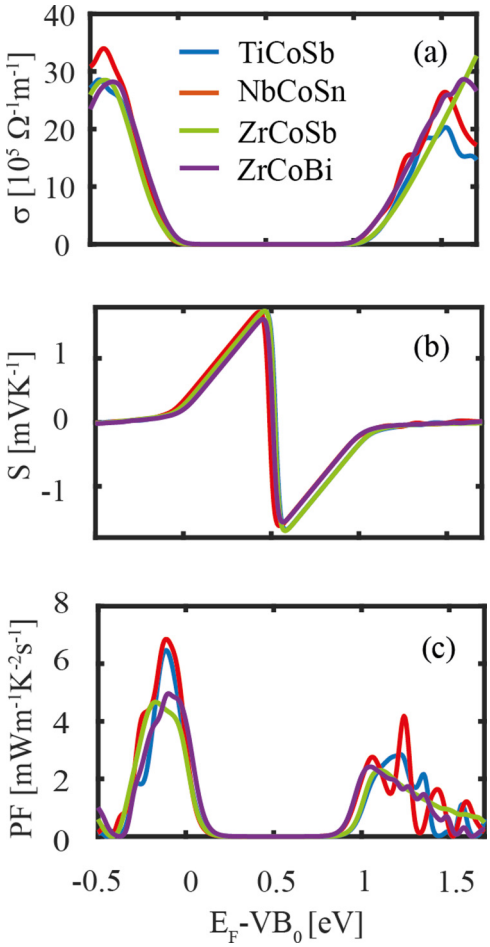

FIG. 13. (a) Conductivity, (b) Seebeck coefficient, and the (c) power factor of NbCoSn, TiCoSb, ZrCoSb, and ZrCoBi for both electrons and holes, calculated using BoltzTraP, employing the constant relaxation time approximation with $\tau = 10^{-14}$ s.

By setting the TD function given by Eq. (C2) to be larger than what is given by Eq. (C1), we find the condition of the mass of B1 compared to that of B2 and B3 for TD improvement as

$$\frac{m_1^{1/2}\,E^{3/2} + m_2^{1/2}\,E^{3/2} + m_3^{1/2}\,E^{3/2}}{m_1^{3/2}\,E^{1/2} + m_2^{3/2}\,E^{1/2} + m_3^{3/2}\,E^{1/2}} > \frac{m_1^{1/2}\,E^{3/2}}{m_1^{3/2}\,E^{1/2}} \quad \text{(C3)}$$

$$\Rightarrow m_1 > \frac{m_2^{3/2} + m_3^{3/2}}{m_2^{1/2} + m_3^{1/2}}. \quad \text{(C4)}$$

APPENDIX D: CALCULATION OF TRANSPORT COEFFICIENTS OF HALF-HEUSLERS

Figure 13 compares the conductivity, Seebeck coefficient, and the power factor for the half-Heuslers NbCoSn, TiCoSb, ZrCoSb, and ZrCoBi, under a constant relaxation time of 10^{-14} s. They all have similar power factors, but TiCoSb and NbCoSn are slightly better when the p-type power factor is considered.

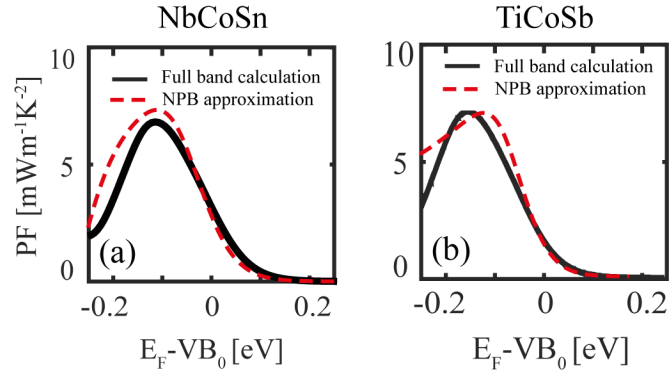

FIG. 14. Comparison of results from the nonparabolic band (NPB) approximation (red dashed lines) and numerical full-band calculations (black solid lines) using BoltzTraP, under the constant relaxation time approximation with $\tau = 10^{-14}$ s, for (a) NbCoSn and (b) TiCoSb.

APPENDIX E: COMPARISON OF THE NONPARABOLIC BAND (NPB) APPROXIMATION WITH THE FULL-BAND CALCULATIONS

The outcome of the NPB approximation is compared with the full-band (DFT derived) results obtained from BoltzTraP calculations, where no approximation about the band shape is made. The NPB parameters used for Figs. 14(a) and 4(b) are given in Figs. 5(b) and 15(b), respectively. The left and right figures show the comparison for NbCoSn and TiCoSb, respectively. Black solid lines are power factor results calculated using the full band structure with BoltzTraP while the red dashed lines are calculated using the NPB approximation and our Boltzmann transport codes. A good match is observed between the two models, indicating the validity of the NPB approximation for the relevant energies under consideration, when the NPB parameters used are extracted from DFT calculated bands.

APPENDIX F: THERMOELECTRIC COEFFICIENTS FOR TICOSB UNDER THE NPB APPROXIMATION

In this Appendix we examine the possibility of improving the power factor by using band alignment in TiCoSb, as shown in Fig. 15, using nonparabolic bands extracted from the DFT band structure. The Fermi surface of TiCoSb at energy 0.1 eV below the VB_0 is shown in Fig. 15(a). The two bands at L point (L_1 and L_2) are only 40 meV below VB_0, which is not a significant separation. Therefore, we would not expect significant improvements upon aligning those bands. We still perform this analysis, however, to demonstrate that the trends here are different compared to what observed in the main text for NbCoSn, and that in this case one observed in a real material the peculiar nonmonotonic trend that is shown in Fig. 3(e). In Fig. 15(b) we present the NPB approximation parameters that describe bands at L point (L_1 and L_2) and Γ point (Γ_1, Γ_2, and Γ_3) assuming the transport to be in the [100] direction. Again, to verify the accuracy of the NPB approximation for TiCoSb, we compare in Appendix E the PFs of the band structure we constructed [Fig. 15(c)]

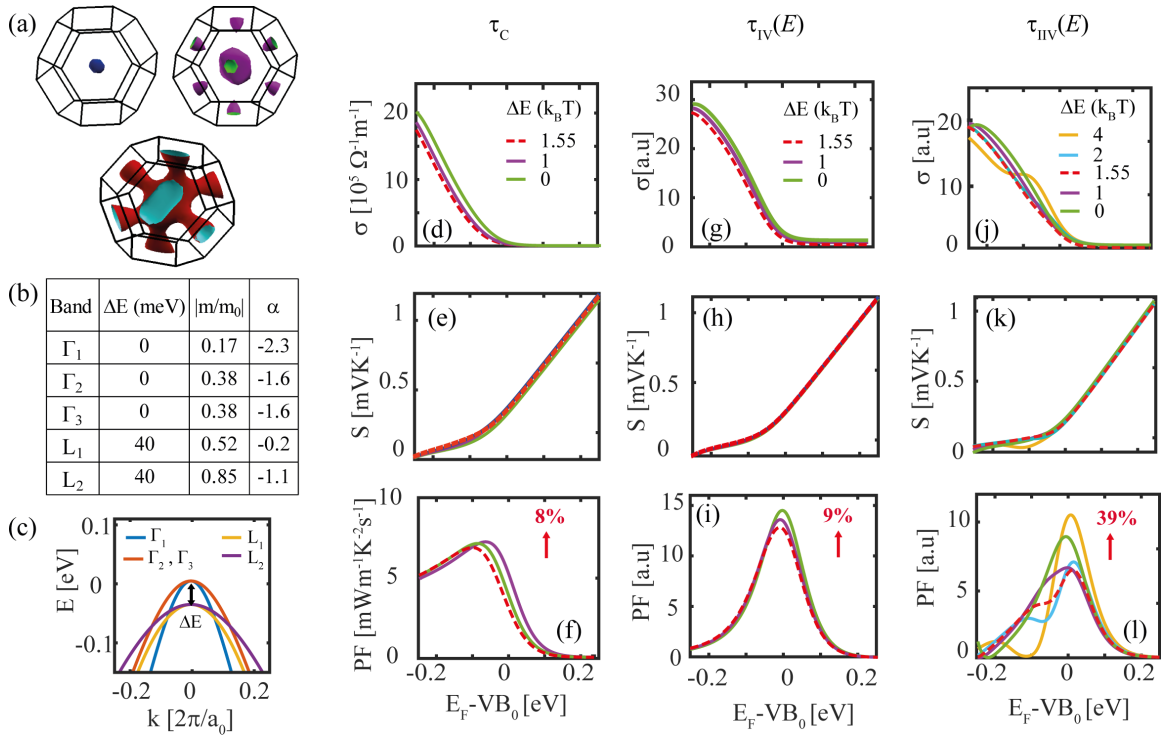

FIG. 15. Thermoelectric coefficients for band alignment in TiCoSb described using the nonparabolic band (NPB) approximation, under three different scattering scenarios. (a) The Fermi surface of TiCoSb at 0.1 eV below VB_0. (b) NPB parameters calculated for valence bands at Γ (Γ_1, Γ_2, and Γ_3) and L (L_1 and L_2) valleys, assuming transport in the [100] direction. (c) The resulting TiCoSb bands extracted using the NPB approximation. The energy position of bands L_1 and L_2 are shifted (in units of k_BT) until it is fully aligned with the VB_0. Column-wise: (d)–(f) Thermoelectric coefficients (σ, S, and PF) calculated using the NPB approximation for TiCoSb under constant rate of scattering (τ_C). (g)–(i) σ, S, and PF under intraband\intravalley scattering only [$\tau_{IV}(E)$]. (j)–(l) σ, S, and PF under inter- and intraband\inter- and intravalley scattering [$\tau_{IIV}(E)$]. The percentage improvement given is the peak-to-peak improvement between $\Delta E = 0$ and $\Delta E = 1.55\,k_BT$ (given by the yellow solid lines and red dashed lines, respectively).

with a fully numerical calculation done on a DFT derived band structure using BoltzTrap and found good agreement between two methods within -0.2 eV ($8\,k_BT$ into the valence band, which is sufficient for our study). Beyond -0.2 eV, PF calculated for the two methods deviate, since the shape of the actual band structure diverges from the NPB shape at higher energies.

Now we move on to calculate thermoelectric parameters for TiCoSb under the NPB approximation for different scattering scenarios (τ_C [Figs. 15(d)–15(f)], $\tau_{IV}(E)$ [Figs. 15(g)–15(i)], and $\tau_{IIV}(E)$ [Figs. 15(j)–15(l)]), under different alignment levels in units of k_BT. The results for the original band structure, before attempting any alignment, is shown by the dashed red lines. The bands we are aligning have higher masses than the bands already aligned. This is the favorable PF improvement condition under a constant rate of scattering and and moderate improvements of $\approx 8\%$ are observed. Moderate improvements to the conductivity and hence to the power factor can also be observed in second scattering scenarios. The improvements are small, however, because $\Delta E = 1.55\,k_BT$, only, and on the other hand, no significant variation is observed in the Seebeck coefficient. The largest improvement (of $\approx 39\%$) is observed when bands are close together, but not fully aligned (yellow lines) under $\tau_{IIV}(E)$. This is a combined effect of increase in conductivity by bringing another band together, but without increasing yet scattering from the light band into the heavy band, while also slightly increases the Seebeck coefficient due to the presence of the second band, i.e., the band alignment is fine tuned as in the situation described in Fig. 3(e).

[1] D. Beretta, N. Neophytou, J. M. Hodges, M. G. Kanatzidis, D. Narducci, M. Martin-Gonzalez, M. Beekman, B. Balke, G. Cerretti, W. Tremel *et al.*, Mater. Sci. Eng. Rep. (2018), doi: 10.1016/j.mser.2018.09.001.

[2] L. E. Bell, Science **321**, 1457 (2008).

[3] A. Shakouri, Annu. Rev. Mater. Res. **41**, 399 (2011).

[4] K. Koumoto, R. Funahashi, E. Guilmeau, Y. Miyazaki, A. Weidenkaff, Y. Wang, and C. Wan, J. Am. Ceram. Soc. **96**, 1 (2013).

[5] X. Zhang and L.-D. Zhao, J. Mater. **1**, 92 (2015).

[6] J. Yang, H. Li, T. Wu, W. Zhang, L. Chen, and J. Yang, Adv. Funct. Materiom. **18**, 2880 (2008).

[7] L. Xi, J. Yang, L. Wu, J. Yang, and W. Zhang, J. Materiom. **2**, 114 (2016).

[8] L. Huang, Q. Zhang, B. Yuan, X. Lai, X. Yan, and Z. Ren, Mater. Res. Bull. **76**, 107 (2016).

[9] A. Page, P. Poudeu, and C. Uher, J. Materiom. **2**, 104 (2016).

[10] W. Xie, A. Weidenkaff, X. Tang, Q. Zhang, J. Poon, and T. Tritt, Nanomaterials **2**, 379 (2012).

[11] J.-W. G. Bos and R. A. Downie, J. Phys.: Condens. Matter **26**, 433201 (2014).

[12] F. Casper, T. Graf, S. Chadov, B. Balke, and C. Felser, Semicond. Sci. Technol. **27**, 063001 (2012).

[13] S. Chen and Z. Ren, Mater. Today **16**, 387 (2013).

[14] J. P. Heremans, V. Jovovic, E. S. Toberer, A. Saramat, K. Kurosaki, A. Charoenphakdee, S. Yamanaka, and G. J. Snyder, Science **321**, 554 (2008).

[15] L.-D. Zhao, S.-H. Lo, Y. Zhang, H. Sun, G. Tan, C. Uher, C. Wolverton, V. P. Dravid, and M. G. Kanatzidis, Nature (London) **508**, 373 (2014).

[16] B. Wölfing, C. Kloc, J. Teubner, and E. Bucher, Phys. Rev. Lett. **86**, 4350 (2001).

[17] H. Kleinke, Chem. Mater. **22**, 604 (2009).

[18] G. Nolas, J. Cohn, G. Slack, and S. Schujman, Appl. Phys. Lett. **73**, 178 (1998).

[19] B. Sales, D. Mandrus, and R. K. Williams, Science **272**, 1325 (1996).

[20] G. Nolas, D. Morelli, and T. M. Tritt, Annu. Rev. Mater. Sci. **29**, 89 (1999).

[21] G. J. Snyder and E. S. Toberer, in *Materials For Sustainable Energy: A Collection of Peer-Reviewed Research and Review Articles from Nature Publishing Group* (World Scientific, Singapore, 2011), pp. 101–110.

[22] L. Zhao, H. Wu, S. Hao, C.-I. Wu, X. Zhou, K. Biswas, J. He, T. P. Hogan, C. Uher, C. Wolverton *et al.*, Energy Environ. Sci. **6**, 3346 (2013).

[23] G. Tan, L.-D. Zhao, F. Shi, J. W. Doak, S.-H. Lo, H. Sun, C. Wolverton, V. P. Dravid, C. Uher, and M. G. Kanatzidis, J. Am. Chem. Soc. **136**, 7006 (2014).

[24] Y. Pei, X. Shi, A. LaLonde, H. Wang, L. Chen, and G. J. Snyder, Nature (London) **473**, 66 (2011).

[25] Y. Tang, Z. M. Gibbs, L. A. Agapito, G. Li, H.-S. Kim, M. B. Nardelli, S. Curtarolo, and G. J. Snyder, Nat. Mater. **14**, 1223 (2015).

[26] P. Norouzzadeh and D. Vashaee, Sci. Rep. **6**, 22724 (2016).

[27] S. Li, H. Zhao, H. Zhang, G. Ren, N. Liu, D. Li, C. Yang, S. Jin, D. Shang, W. Wang *et al.*, RSC Adv. **5**, 99065 (2015).

[28] G. Tan, L.-D. Zhao, and M. G. Kanatzidis, Chem. Rev. **116**, 12123 (2016).

[29] K. Imasato, S. D. Kang, S. Ohno, and G. J. Snyder, Mater. Horizons **5**, 59 (2018).

[30] W. Liu, X. Tan, K. Yin, H. Liu, X. Tang, J. Shi, Q. Zhang, and C. Uher, Phys. Rev. Lett. **108**, 166601 (2012).

[31] S. Thompson, S. Suthram, Y. Sun, G. Sun, S. Parthasarathy, M. Chu, and T. Nishida, in *IEDM Technical Digest* (IEEE, 2006) pp. 1–4.

[32] P. W. Leu, A. Svizhenko, and K. Cho, Phys. Rev. B **77**, 235305 (2008).

[33] Q. Yan, H. Chen, W. Zhou, H. H. Hng, F. Y. C. Boey, and J. Ma, Chem. Mater. **20**, 6298 (2008).

[34] N. Neophytou and H. Kosina, Nano Lett. **10**, 4913 (2010).

[35] N. Neophytou, M. Wagner, H. Kosina, and S. Selberherr, J. Electron. Mater. **39**, 1902 (2010).

[36] D. Misra, A. Bhardwaj, and S. Singh, J. Mater. Chem. A **2**, 11913 (2014).

[37] J. Zhou, H. Zhu, T.-H. Liu, Q. Song, R. He, J. Mao, Z. Liu, W. Ren, B. Liao, D. J. Singh *et al.*, Nat. Commun. **9**, 1 (2018).

[38] C. Fu, T. Zhu, Y. Pei, H. Xie, H. Wang, G. J. Snyder, Y. Liu, Y. Liu, and X. Zhao, Adv. Energy Mater. **4**, 1400600 (2014).

[39] C. Fu, S. Bai, Y. Liu, Y. Tang, L. Chen, X. Zhao, and T. Zhu, Nat. Commun. **6**, 8144 (2015).

[40] T. Graf, C. Felser, and S. S. Parkin, Prog. Solid State Chem. **39**, 1 (2011).

[41] T. J. Scheidemantel, C. Ambrosch-Draxl, T. Thonhauser, J. V. Badding, and J. O. Sofo, Phys. Rev. B **68**, 125210 (2003).

[42] A. Berche and P. Jund, Materials **11**, 868 (2018).

[43] M. Lundstrom, *Fundamentals of Carrier Transport* (Cambridge University Press, Cambridge, 2009).

[44] D. Pshenay-Severin and M. Fedorov, Phys. Solid State **52**, 1342 (2010).

[45] E. Witkoske, X. Wang, M. Lundstrom, V. Askarpour, and J. Maassen, J. Appl. Phys. **122**, 175102 (2017).

[46] G. Mahan and J. Sofo, Proc. Natl. Acad. Sci. **93**, 7436 (1996).

[47] N. Neophytou and H. Kosina, Phys. Rev. B **83**, 245305 (2011).

[48] G. K. Madsen and D. J. Singh, Comput. Phys. Commun. **175**, 67 (2006).

[49] P. Giannozzi, S. Baroni, N. Bonini, M. Calandra, R. Car, C. Cavazzoni, D. Ceresoli, G. L. Chiarotti, M. Cococcioni, I. Dabo *et al.*, J. Phys.: Condens. Matter **21**, 395502 (2009).

[50] M. Zahedifar and P. Kratzer, Phys. Rev. B **97**, 035204 (2018).

[51] L.-D. Zhao, G. Tan, S. Hao, J. He, Y. Pei, H. Chi, H. Wang, S. Gong, H. Xu, V. P. Dravid *et al.*, Science **351**, 141 (2016).

[52] D. J. Singh, Phys. Rev. B **81**, 195217 (2010).

[53] H. Zhu, R. He, J. Mao, Q. Zhu, C. Li, J. Sun, W. Ren, Y. Wang, Z. Liu, Z. Tang *et al.*, Nat. Commun. **9**, 2497 (2018).

[54] See Supplemental Material at http://link.aps.org/supplemental/10.1103/PhysRevB.99.195202 for a comparison of the calculated conductivity with experimental data for TiCoSb, a study of electron relaxation through electron-phonon interactions for TiCoSb and ZrCoSb, and band structures with spin-orbit coupling for TiCoSb, ZrCoSb and NbCoSn.

[55] T. Wu, W. Jiang, X. Li, S. Bai, S. Liufu, and L. Chen, J. Alloys Compd. **467**, 590 (2009).

[56] T. Wu, W. Jiang, X. Li, Y. Zhou, and L. Chen, J. Appl. Phys. **102**, 103705 (2007).

[57] S. Poncé, E. R. Margine, C. Verdi, and F. Giustino, Comput. Phys. Commun. **209**, 116 (2016).

[58] J. Corps, P. Vaqueiro, A. Aziz, R. Grau-Crespo, W. Kockelmann, J.-C. Jumas, and A. V. Powell, Chem. Mater. **27**, 3946 (2015).

[59] S. Roychowdhury, U. S. Shenoy, U. V. Waghmare, and K. Biswas, J. Mater. Chem. C **5**, 5737 (2017).

[60] M. Rudan, *Physics of Semiconductor Devices* (Springer, Berlin, 2015).

[61] B. Qiu, Z. Tian, A. Vallabhaneni, B. Liao, J. M. Mendoza, O. D. Restrepo, X. Ruan, and G. Chen, Europhys. Lett. **109**, 57006 (2015).

[62] D. Pshenay-Severin, Y. Ivanov, and A. Burkov, J. Phys.: Condens. Matter **30**, 475501 (2018).

[63] C. Jeong and M. Lundstrom, J. Electron. Mater. **40**, 738 (2011).

[64] G. Capellini, C. Reich, S. Guha, Y. Yamamoto, M. Lisker, M. Virgilio, A. Ghrib, M. El Kurdi, P. Boucaud, B. Tillack *et al.*, Opt. Express **22**, 399 (2014).

[65] I. Jeong, J. Kwon, C. Kim, and Y. J. Park, Opt. Express **22**, 5927 (2014).

[66] Y. Y. H. G. F. W. Low, Kain Lu, and Y.-C. Yeo, J. Appl. Phys. **112**, 103715 (2012).

[67] M. Zhou, G. J. Snyder, L. Li, and L.-D. Zhao, Inorg. Chem. Front. **3**, 1449 (2016).

[68] A. D. LaLonde, Y. Pei, H. Wang, and G. J. Snyder, Mater. Today **14**, 526 (2011).